# Heat transfer and fluid flow in additive manufacturing

A. Raghavan, H. L. Wei, T. A. Palmer, and T. DebRoy

---

### Articles you may be interested in

Heat transfer and material flow during laser assisted multi-layer additive manufacturing
J. Appl. Phys. **116**, 124905 (2014); 10.1063/1.4896751

Mathematical modeling of heat transfer, fluid flow, and solidification during linear welding with a pulsed laser beam
J. Appl. Phys. **100**, 034903 (2006); 10.1063/1.2214392

Numerical simulation of heat transfer and fluid flow in coaxial laser cladding process for direct metal deposition
J. Appl. Phys. **100**, 024903 (2006); 10.1063/1.2209807

Heat transfer and fluid flow in laser microwelding
J. Appl. Phys. **97**, 084909 (2005); 10.1063/1.1873032

Modeling of heat transfer and fluid flow during gas tungsten arc spot welding of low carbon steel
J. Appl. Phys. **93**, 3022 (2003); 10.1063/1.1540744

---

# Heat transfer and fluid flow in additive manufacturing

A. Raghavan, H. L. Wei, T. A. Palmer, and T. DebRoy
*Department of Materials Science and Engineering, Pennsylvania State University, University Park, Pennsylvania 16802*

In laser-based direct energy deposition additive manufacturing, process control can be achieved through a closed loop control system in which thermal sensing of the melt pool surface is used to adjust laser processing parameters to maintain a constant surface geometry. Although this process control technique takes advantage of important in-process information, the conclusions drawn about the final solidification structure and mechanical properties of the deposited material are limited. In this study, a validated heat transfer and fluid flow laser welding model are used to examine how changes in processing parameters similar to those used in direct energy deposition processes affect the relationships between top surface and subsurface temperatures and solidification parameters in Ti-6Al-4V. The similarities between the physical processes governing laser welding and laser-based additive manufacturing make the use of a laser welding model appropriate. Numerical simulations show that liquid pools with similar top surface geometries can have substantially different penetration depths and volumes. Furthermore, molten pool surface area is found to be a poor indicator of the cooling rate at different locations in the melt pool and, therefore, cannot be relied upon to achieve targeted microstructures and mechanical properties. It is also demonstrated that as the build temperature increases and the power level is changed to maintain a constant surface geometry, variations in important solidification parameters are observed, which are expected to significantly impact the final microstructure. Based on the results, it is suggested that the conclusions drawn from current experimental thermography control systems can be strengthened by incorporating analysis through mathematical modeling. © *2013 Laser Institute of America.*

Key words: additive manufacturing, direct energy metal deposition, feedback image sensing, control, finite difference modeling

## I. INTRODUCTION

Laser-based direct energy deposition additive manufacturing (AM) processes allow for the fabrication of near net-shape and net-shape three-dimensional structural components from a powder precursor material in a layer-by-layer manner.[1–4] AM is an attractive process because one can rapidly produce near net-shape components without significant material loss due to machining or other follow-on activities and without the long lead times needed to receive cast or forged products. These systems also allow the user to alternate efficiently between a wide assortment of parts utilizing computer-aided design models, and generate complex features with a high degree of geometric precision.

Additive manufacturing can be used with an extensive range of industrially relevant materials, including titanium, nickel, and stainless steel alloys.[5,6] During the processing of parts made from these materials, the powder precursor undergoes rapid melting and solidification as each subsequent layer is deposited during the build process. As the build progresses, these previously deposited layers then experience large temperature gradients and enhanced thermal stresses during the entirety of the part build. To ensure consistent material properties in the final part, process control is required.

One means for process control involves utilizing real-time thermal sensing of the molten pool surface to modulate laser processing parameters and maintain a consistent size and shape.[7–10] Although these feedback methods are designed to ensure consistency in the melt, the complexity of the AM process introduces a great deal of uncertainty as to how the entire deposit behaves during the span of the build. While the deposit is molten, the material undergoes significant convective flow, potential alloying element vaporization, and steep thermal gradients as it is rapidly heated by the laser. After solidification, the build undergoes complex thermal cycling as new material is placed on top of previously deposited material.

The physical processes that govern the direct energy deposition AM process and contribute to complex processing conditions are similar to those experienced during laser welding.[11] Such similarities allow for the use of laser welding as a proxy for understanding the AM process. Previous efforts directed at the modeling of laser welds in the same laser power ranges used in AM have shown that knowledge of the top surface pool geometry and temperature profiles alone cannot provide sufficient data to fully characterize the subsurface molten pool shape and thermal cycles during processing.[12–15]

In this study, a well-tested, three-dimensional numerical model is used to analyze how necessary changes in laser processing parameters to maintain a target melt geometry can impact thermal cycles, fluid flow, and solidification during laser deposition of Ti-6Al-4V. It is shown that despite similarities in molten pool top surface geometry, penetration

depth, and melt volume can be drastically different. The reasons for such differences are explained using the dimensionless Peclet (Pe) number and an understanding of how changes in temperature gradients along the melt pool surface impact Marangoni flow,[16,17] which influences the penetration depth under different processing conditions.

Simulations are also performed to understand how changing the laser power during processing to maintain a constant molten pool geometry in response to changes in build temperature can impact the solidification microstructure. The build temperature is defined here as the current substrate temperature as heat is retained in previously deposited material from the progressive addition of layers. It is shown that solidification parameters, such as the cooling rate, temperature gradient, and solidification rate, can vary significantly for processing conditions that exhibit similar molten pool top surface geometries. Finally, thermal cycles are calculated at a number of locations within the molten pool to demonstrate how numerical simulations add value to experimental thermography to understand the melting and solidification behavior.

## II. MATHEMATICAL MODEL

A three-dimensional laser welding heat transfer and fluid flow mathematical model was used to calculate the temperature profiles, fluid flow velocities, and molten pool geometry experienced during laser processing of a Ti-6Al-4V alloy. The material properties and processing parameters used in the calculations are shown in Table I.[18–20] Since the details of the numerical model are available elsewhere,[21,22] only a brief description is presented here. The model uses a Cartesian coordinate system and the control volume method[23] to calculate the fluid velocities and enthalpy by solving the conservation equations for mass (1), momentum (2), and energy (3)

$$\frac{\partial(\rho u_i)}{\partial x_i} = 0, \tag{1}$$

TABLE I. Data used for the calculations.

| Material property/parameter | Value | Reference |
|---|---|---|
| Absorption coefficient | 0.27 | 19 |
| Beam radius (mm)[a] | 0.2 | — |
| Coefficient of thermal expansion (K$^{-1}$) | $1.1 \times 10^{-5}$ | 18 |
| Density (kg m$^{-3}$) | 4000 | 18 |
| Effective thermal conductivity of liquid (J m$^{-1}$ s$^{-1}$ K$^{-1}$) | 141 | 18 and 20 |
| Effective viscosity (kg m$^{-1}$ s$^{-1}$) | 0.0343 | 20 |
| Enthalpy of solid at melting point (kJ kg$^{-1}$) | 1121 | 18 |
| Enthalpy of liquid at melting point (kJ kg$^{-1}$) | 1490 | 18 |
| Laser power distribution factor $f$[b] | 1.5 | — |
| Liquidus temperature (K) | 1828 | 18 |
| Solidus temperature (K) | 1928 | 18 |
| Specific heat of liquid (J kg$^{-1}$ K$^{-1}$) | 610 | 18 |
| Specific heat of solid (J kg$^{-1}$ K$^{-1}$) | 700 | 18 |
| Temperature coefficient of surface tension (N m$^{-1}$ K$^{-1}$) | −0.28 | 18 |
| Thermal conductivity of solid (J m$^{-1}$ s$^{-1}$ K$^{-1}$) | 20 | 18 |

[a]Values estimated based on typical AM laser beam radius.
[b]Value based on Gaussian beam distribution.

where $\rho$ is the density, $u_i$ is the velocity component along the $i$ direction, and $x_i$ is the distance along the $i = 1$, 2, and 3 directions

$$\frac{\partial(\rho u_j)}{\partial t} + \frac{\partial(\rho u_j u_i)}{\partial x_i} = \frac{\partial}{\partial x_i}\left(\mu \frac{\partial u_j}{\partial x_i}\right) + S_j, \tag{2}$$

where $u_j$ is the velocity component along the $j$ direction, $t$ is the time, $\mu$ is the effective viscosity, and $S_j$ is a source term for the $j$ component momentum equation

$$\rho \frac{\partial(h)}{\partial t} + \frac{\partial(\rho u_i h)}{\partial x_i} = \frac{\partial}{\partial x_i}\left(\frac{k}{C_p}\frac{\partial h}{\partial x_i}\right) - \rho \frac{\partial(\Delta H)}{\partial t} - \rho \frac{\partial(u_i \Delta H)}{\partial x_i}, \tag{3}$$

where $h$ is the sensible heat, $C_p$ is the specific heat, and $\Delta H$ is the latent heat content. Each equation has been discretized by integrating over the control volumes and iteratively solved for the dependent variables using the tridiagonal matrix algorithm.[23]

The power density distribution for the laser on the top surface of the computational domain was determined using the following expression:

$$H_{in} = \frac{qf\eta}{r_b^2}\exp\left(-\frac{f(x^2 + y^2)}{r_b^2}\right), \tag{4}$$

where $q$ is the laser power, $f$ is the power distribution factor, $\eta$ is the laser energy absorptivity at the work piece, $r_b$ is laser beam radius, and $x$ and $y$ are the coordinates on the top surface used to calculate the incoming heat at that particular location. Due to symmetry, only half the work piece was considered and nonuniform grid spacing was used to maintain computational accuracy with finer grid spacing below the heat source. The top surface is assumed to be flat, and the velocity boundary conditions and convergence criteria are specified elsewhere.[24,25]

The absorption of a laser beam by the work piece during additive manufacturing is affected by powder feeding in several ways. The powder particle size distribution and feed rate, laser beam wavelength and its power density distribution will affect the energy absorption rate. Therefore, because of the large number of variables involved in the interaction between the laser beam and the work piece, a general model for the laser beam absorption to describe all possible modes of powder feeding during additive manufacturing is unlikely to accurately capture the physical processes that take place. Two specific situations can be considered to illustrate the differences in the interaction of the laser beam with the work piece. In the first case, the laser beam interacts with a powder bed and the absorption of the beam occurs via multiple reflections within the powder bed. As a result, the energy absorption rate is much higher than that encountered in the absorption of the laser beam by the Fresnel absorption on a flat liquid surface. In the second case, the powder feed rate is assumed to be low and the powder is fed directly behind the laser beam on the liquid pool surface, so that the laser beam essentially interacts with the liquid surface and the extent of absorption is roughly equal to that of Fresnel absorption.
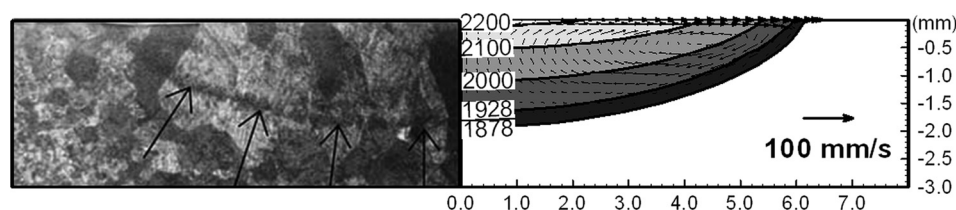
FIG. 1. Experimental and calculated cross sections of a Ti-6Al-4V gas tungsten arc weld using 2.13 MJ m$^{-1}$ heat input. The arrows show the location of the fusion zone boundary in the micrograph (Ref. 25).

In most other cases, the absorption of laser beam is between the first and the second cases. In laser cladding, it has been shown that the injected powder particles as well as the Brewster angle of the previously clad material can impact the amount of laser power absorbed at the substrate.[26] It has also been shown that preplaced powder particles can increase the absorptivity due to the surface area to volume ratio of the powders as well as multiple reflections between particles.[27] In fact, the previous studies show that a quantitative determination of the extent of laser beam absorption is fairly complicated and deserves a separate study. In order to focus on the objectives of this work, it has been assumed that the powder is fed on the liquid pool surface behind the laser beam and the laser interacts directly with the molten pool surface. Consideration of this situation allows assessment of the process control issues without complications of the possible differences in the energy absorption rates in different cases resulting from the large number of variables that affect the interaction between the laser beam and the powder during additive manufacturing. Furthermore, the Brewster effect is not important for this situation, since the beam is directed normal to the molten pool surface.

## III. RESULTS AND DISCUSSION

For this work, the model was validated using independently obtained experimental results for a gas tungsten arc weld (GTAW) produced on a Ti-6Al-4 V alloy.[28] The GTAW process in this case will be governed by similar heat transfer characteristics as those found in both conduction mode laser welding and additive manufacturing and is therefore an appropriate geometry for model validation. Figure 1 shows 100% agreement in depth and greater than 98% agreement in width between the calculated and experimental molten pool geometry. The experimental depth and half-width of the weld pool were 2.0 and 6.3 mm, respectively, compared with the calculated depth and half-width 2.0 and 6.2 mm, respectively. Table II also shows excellent agreement

TABLE II. Comparison of the calculated weld pool dimensions with the experimental results.

| Weld no. | Energy/length (MJ m$^{-1}$) | Depth (mm) | | Half-width | |
|---|---|---|---|---|---|
| | | Exp. | Cal. | Exp. | Cal. |
| 1 | 2.13 | 2.0 | 2.0 | 6.3 | 6.2 |
| 2 | 1.10 | 1.5 | 1.6 | 6.0 | 6.0 |
| 3 | 0.55 | 1.1 | 1.1 | 4.8 | 4.8 |

between the calculated and experimental pool geometries for a wide range of processing conditions.

Using this experimentally validated model, laser processing of a Ti-6Al-4V alloy was simulated to demonstrate the limitations of using temperature sensing of the molten pool top surface geometry for process control. Figures 2(a) and 2(b) show the molten pool top surface geometry when processing at 450 W with a 0.2 mm laser beam radius versus 460 W with a 0.7 mm beam radius. In both cases, the travel speed is 10.6 mm/s. Despite the differences in laser power and beam radius, the two molten pools exhibit the same top surface geometry. With such a large difference in beam radius, however, the melt depths are substantially different, as shown in Figs. 2(c) and 2(d).

When using a higher power density as a result of the smaller beam radius, the melt depth is approximately two times larger. This difference in melt depth is related to the higher peak temperatures observed at the molten pool surface. The peak temperature in the molten pool produced with the higher power density was approximately 2935 versus 2038 K for the lower power density. With a significantly greater peak temperature yet similar top surface pool geometry, the temperature gradients along the top surface are substantially larger when using the higher power density. As a result, the Marangoni force is greater due to the larger spatial variation of surface tension between the middle and the periphery of the molten pool, and the fluid flow velocities within the molten region are ~10× larger. As fluid flow velocities increase, the heat transfer dynamics affect the molten pool shape and size.

The dimensionless heat transfer Pe number is a ratio of heat transferred by convection to heat transferred by conduction in the molten pool. It is used to evaluate the dominant heat transfer mechanism within the melt and is calculated as follows:

$$Pe = \frac{convection}{conduction} = \frac{u\rho\,C_p\,\Delta T}{k\,\Delta T/L_R} = \frac{u\rho\,C_p\,L_R}{k}, \quad (5)$$

where $u$ is the magnitude of the velocity, $\Delta T$ is the difference between the peak temperature and liquidus temperature, $L_R$ is the characteristic length defined here as the molten pool width, and all other terms have been previously defined. The molten pool with the higher power density has a Pe number of approximately 112 versus a Pe of 10 for the lower power density. In both cases, the Pe number is greater than 1, which means that heat transfer is primarily driven by convection. However, with a Pe number that is an order of magnitude larger for the case with higher power density, heat transfer
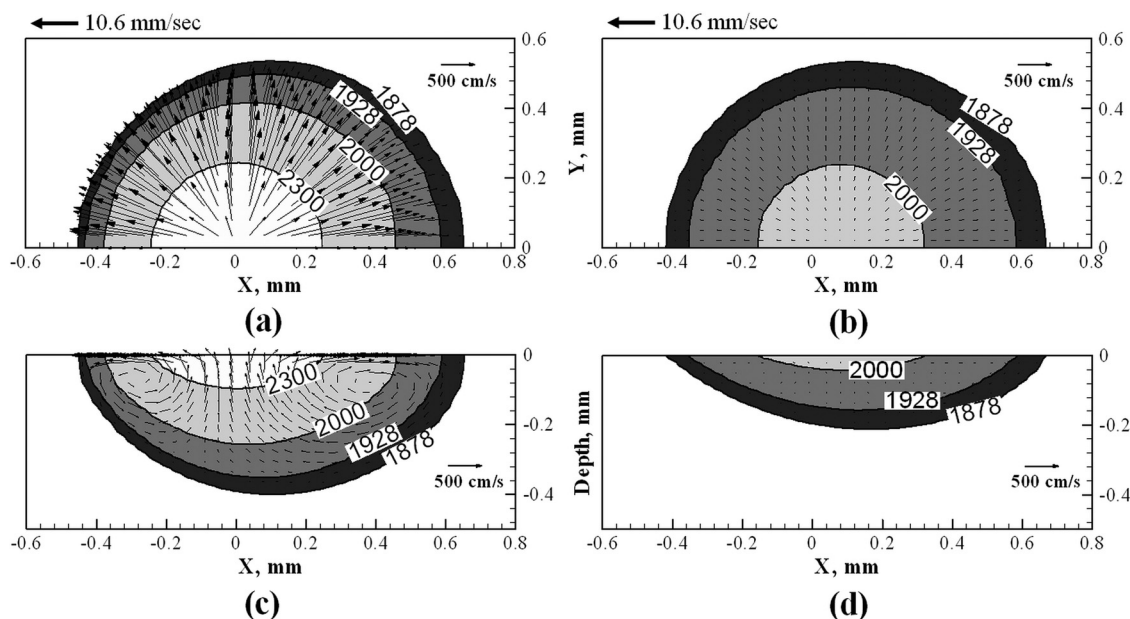
FIG. 2. (a)–(d) Calculated top surface and longitudinal cross sections of molten pool produced with (a) and (c) 450 W laser power with 0.2 mm laser beam radius and (b) and (d) 460 W laser power with 0.7 mm beam radius in Ti-6Al-4 V.

by convection plays a much larger role. As a result, a substantially larger penetration depth is observed.

Despite similar top surface geometries for the two processing conditions, the overall pool geometries vary considerably. Furthermore, the two cases demonstrate that since a clear correlation between the peak temperature and molten pool geometry is not readily apparent, it may be difficult to accurately implement process control based solely on thermal imaging of the temperature profiles on the top surface of the molten pool. Therefore, monitoring the top surface dimensions of the melt pool can provide misleading information to predict the penetration depth.

In addition to looking at molten pool geometry, the model was used to calculate thermal cycles at various locations within the melt pool. Figure 3 shows the thermal cycles experienced along the centerline of the molten pool at the surface, 1 mm below the surface and 2 mm below the surface for the two conditions shown in Fig. 2. The thermal cycles are significantly different for the two cases. The cooling rates within the molten region are much higher when processing at a higher power density, which is largely due to the higher peak temperature within the melt. Calculations like these of the thermal cycles can be used to understand the impact on microstructural properties.

In titanium alloys, such as Ti-6Al-4V, it is critical to understand the $\alpha \rightarrow \beta$ transformation in order to predict microstructure. For these two power densities, various positions within the molten region and substrate spend different amounts of time above this transformation temperature. At the lower power density, locations that are 2 mm below the surface do not exceed the solidus temperature, and the time above the $\beta$-transus temperature is approximately 17% less than that observed with the higher power density conditions. This difference in time above the $\beta$-transus can have an impact on the phase ratios and microstructural morphologies. In the cases considered, the substrate was assumed to be at

ambient (298 K) temperature. In AM, the build will undergo thermal cycling as new material is deposited, which will change the substrate temperature during subsequent passes.

In a closed-loop control system, the laser power can be changed to maintain a constant molten pool surface area as the build temperature changes. Mathematical modeling was performed to evaluate the impact of changing laser power to maintain a constant melt surface geometry while accounting for an increase in substrate temperature during subsequent passes. Figure 4 shows the melt formed when using a power level of 300 W and 500 °C build temperature as required to maintain a molten pool length of 1.1 mm and half-width of 0.54.

A comparison can be made between Figs. 2(a) and 2(c) and Figs. 4(a) and 4(b) where molten pool shape is maintained despite changes in power level. With a 500 °C build temperature, for instance, 300 W of laser power is required to produce the same molten pool size versus 450 W with no build temperature. Although maintaining a constant surface area keeps molten pool volume approximately the same, a 33% reduction in laser power is required to maintain the desired molten pool size. This represents a significant reduction in heat input. Reducing the heat input can be beneficial to improve and retain mechanical properties by inhibiting grain growth within the solidified portions of the build. However, changing the heat input to maintain a target melt pool geometry can lead to variations in the solidification microstructure throughout the part.

The implications of changes in heat input required to maintain melt pool surface geometry are evaluated in Fig. 5 using dimensionless numbers. Figure 5 shows a plot of a peak temperature divided by the boiling temperature of Ti-6Al-4V versus a dimensionless heat input. Since there are a number of material properties and processing parameters being considered, the dimensionless value calculated here represents an effective heat input that includes laser beam characteristics and deposition parameters
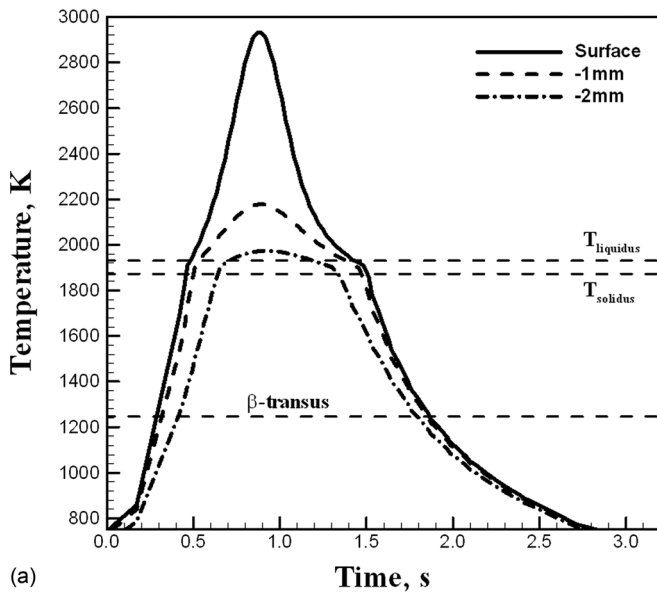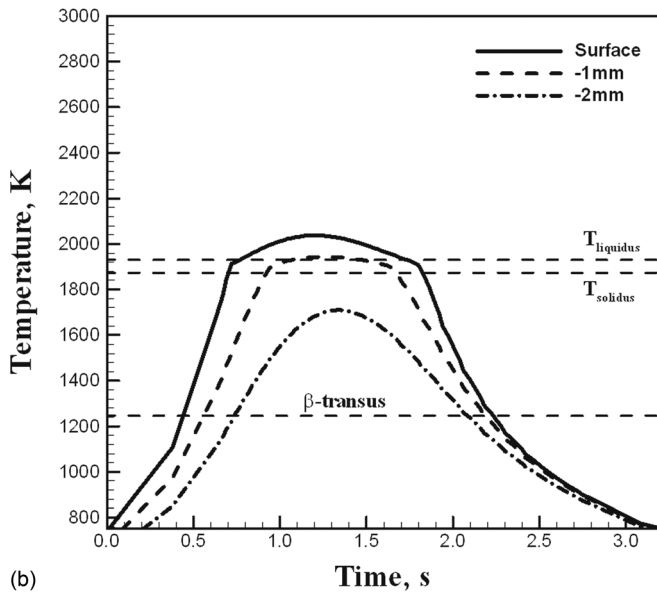
FIG. 3. Temperature profiles at various locations along molten pool surface and within substrate for the two welding conditions: (a) 450 W laser power with 0.2 mm beam radius and (b) 460 W laser power with 0.7 mm laser beam radius with all other parameters identical.

$$N_{HI} = \frac{\dfrac{P\,\eta}{\pi\,r_b^2\,v}}{\rho\,C_{PS}\,(T_L - T_a) + \rho\,L},$$ (6)

where $P$ is the laser power (W), $\eta$ is the absorptivity, $r_b$ is the laser beam radius (m), $v$ is the welding velocity (ms$^{-1}$), $C_{ps}$ is the specific heat of the solid metal (J kg$^{-1}$ K$^{-1}$), $\rho$ is the density (kg m$^{-3}$), $L$ is the latent heat of fusion (J kg$^{-1}$), and $T_L$ and $T_a$ are the liquidus and ambient temperatures (K), respectively. In Fig. 5, it is necessary to reduce the heat input to maintain the same molten pool geometry as the build temperature is increased. The range of build temperatures varies from 700 °C at the lowest heat input to ambient at the highest heat input. As the substrate temperature increases with subsequent passes, a lower heat input is required to maintain the same molten pool geometry, leading to the peak temperature within
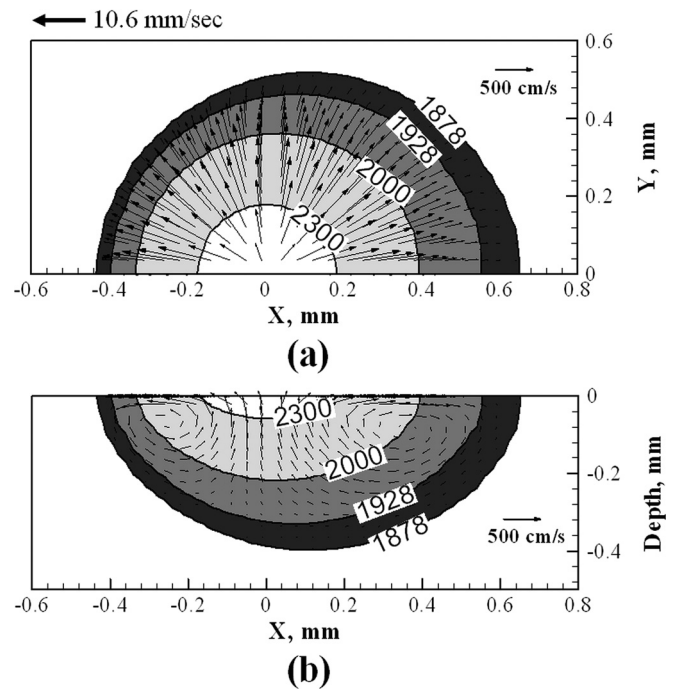


FIG. 4. Molten pool (a) top surface and (b) axial view in direction of welding of when processing with 300 W laser power and 500 °C build temperature.

the melt becoming a smaller fraction of the boiling temperature. With this reduction in peak temperature, changes in the final solidification microstructures can be expected as the build temperature changes, which will impact the mechanical properties of the solidified material.

The solidification microstructure is directly dependent on the solidification rate, $R$, and the temperature gradient, $G$. These values convey important information in their combined forms of $GR$ (cooling rate) and $G/R$. The $G/R$ value will impact the solidification morphology, while the cooling rate ($GR$) value will influence the size of the solidification structure. As the value of $G/R$ increases, the grain morphology changes from equiaxed dendritic to cellular dendritic to cellular. Figures 6(a) and 6(b) shows plots of the cooling rate
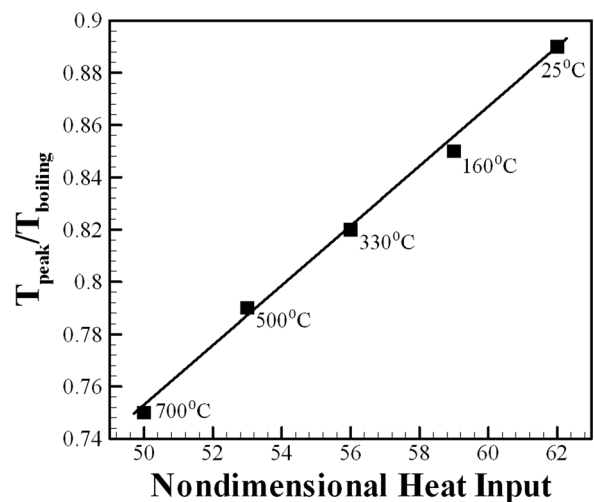


FIG. 5. Plot showing ratio of peak temperature to boiling temperature vs nondimensional heat input. Build temperatures are marked next to each data point.
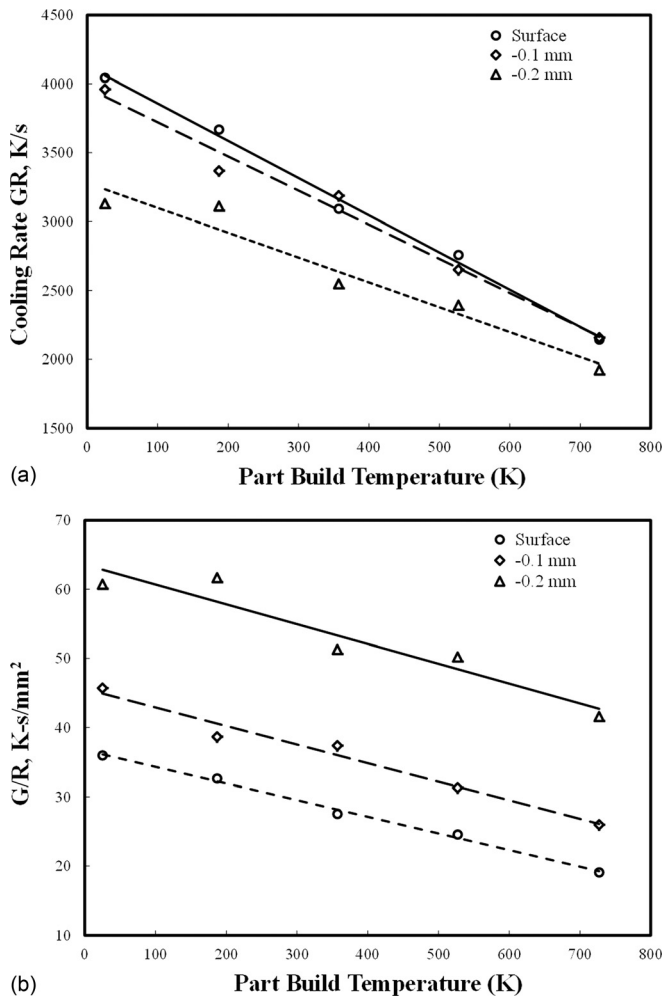
FIG. 6. Plots showing (a) cooling rate and (b) G/R at fusion boundary at surface and specific depths below the surface versus part build temperature.

and *G/R*, respectively, calculated at the weld fusion line at various depths within the substrate versus part build temperature. In the plots shown, the lower net heat input is used for the cases where the build temperature is the highest. When the build temperature is at its highest level, a lower heat input is required to generate the same molten pool geometries. Figure 6 shows that as the build temperature is increased, both the cooling rate and *G/R* value are reduced at all depths within the substrate. When the build temperature is close to ambient and the heat input is at the highest level, the cooling rate and *G/R* values are shown to increase considerably over the values observed when processing at higher part build temperatures. For instance, at the surface of the part, the cooling rate increases 84% when processing at ambient temperature versus 727 °C part build temperature, and the *G/R* value increases by 76%. With such drastic changes in these values, it can be expected that varying the net heat input to compensate for changes in build temperature to maintain a specific molten pool top surface area will result in different solidification structures within the near net-shaped part. Both the scale and morphology of the solidification structure can be predicted by calculating these solidification parameters.

The degree to which the microstructure is altered will depend on the thermal cycles experienced at various locations.
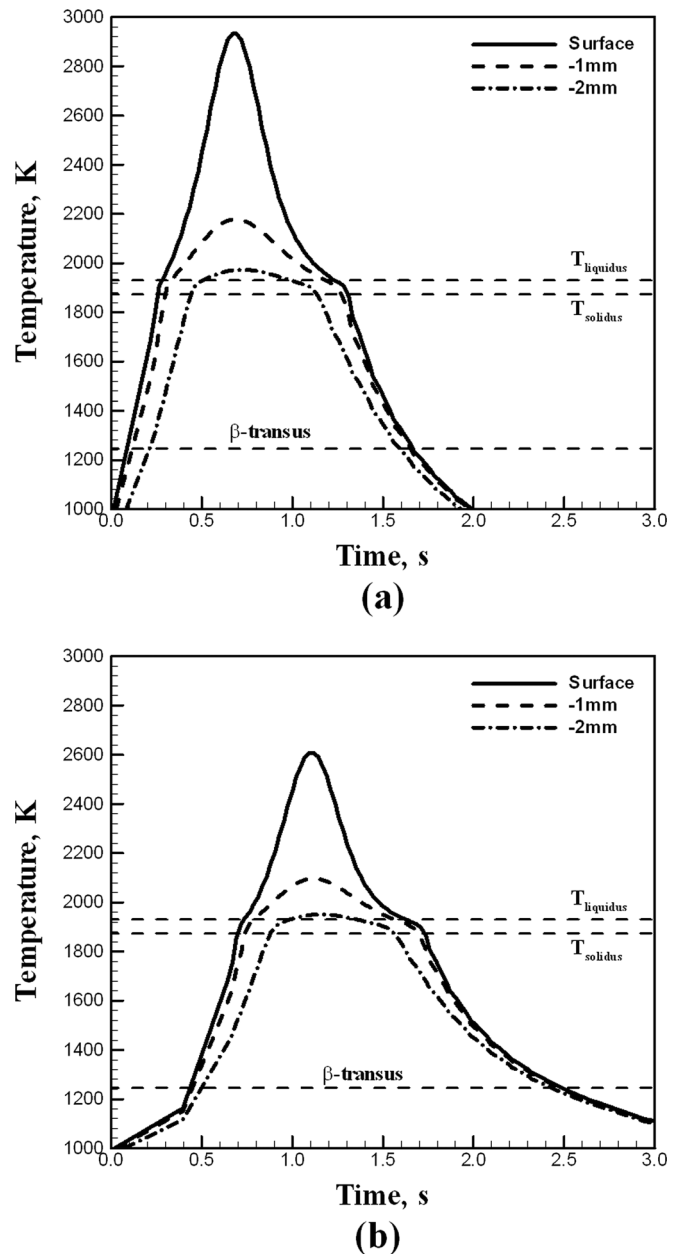


FIG. 7. Temperature profile at various horizontal planes within the molten pool when processing with (a) 450 W laser power and no build temperature and (b) 300 W laser power with 500 °C build temperature.

Figure 7 shows a comparison of the thermal cycles calculated at the surface of the substrate and various depths at the centerline for a 450 W laser power and no increase in build temperature and 300 W laser power assuming a 500 °C increase in build temperature to maintain the same molten pool geometry. By comparing the thermal cycles, it can be observed that the time the material spends above the *β*-transus temperature when experiencing a 500 °C increase in build temperature is ∼ 2 s, which is approximately 25% longer with ambient part build temperature.

The numerical calculations shown here represent qualitative changes in the expected solidification microstructure in response to changes in laser processing parameters to maintain a target molten pool surface area. It would be necessary to consider thermodynamics and kinetics to accurately

predict molten pool solidification morphologies. However, it is important to understand that numerical modeling provides a means to estimate important solidification parameters, and knowing the implications of changes in these values can provide a sound basis for developing more comprehensive real-time control strategies.

Process control feedback based on top surface thermography can be supplemented with phenomenological analysis by numerical models to accurately predict molten pool geometry and temperature profiles to understand microstructure and mechanical properties. By determining the top surface temperature profiles using experimental thermography, numerical models can be validated in real-time and further used to calculate the thermal cycles and temperature gradients within a molten pool beneath the surface. Furthermore, numerical simulations can be used to determine temperature profiles anywhere inside the molten pool to add additional feedback control to the AM process.

## IV. SUMMARY AND CONCLUSIONS

A well-tested laser welding model was used to analyze the impact of using thermography systems to control molten pool geometry in direct energy deposition AM processes. For this analysis, a laser welding model serves as an acceptable surrogate for the AM process due to the similarity in complex physical phenomena governing both processes. Heat transfer and liquid metal flow modeling was used to calculate molten pool shapes and thermal cycles during laser processing of a Ti-6Al-4V alloy to advocate for a more comprehensive control method for AM since feedback control based solely on maintaining a target top surface geometry can be limited. The following conclusions are drawn from the work:

1. Monitoring the top surface melt geometry does not provide sufficient information to accurately predict the melt depth. The top surface molten pool size and shape can be similar for different sets of laser processing parameters despite significant differences in overall molten pool geometry and volume. A reduction in the laser beam radius caused the peak temperature to increase substantially, which led to much higher fluid flow velocities and an increase in molten pool depth by over 100%.

2. Large changes in the power level are required when considering the effect of the interpass build temperatures to maintain a constant melt pool size and shape. By changing the power level to maintain the same top surface geometry in response to variations in substrate build temperature, the molten pool volume experiences little change. However, a decrease in the laser power results in substantially lower peak temperatures within the molten pool that can impact material properties.

3. Solidification parameters, such as the cooling rate and G/R, can vary drastically for molten pools of the same geometry due to changes in net heat input. Although the molten pool size is maintained, the microstructure of the substrate will be affected. A decrease in the net heat input

to maintain a specific molten pool size was shown to increase the time spent above the $\beta$-transus temperature almost 25%, which will likely affect the final solidification microstructure and lead to variations in mechanical properties within the part.

4. To obtain an accurate estimation of molten pool shape, thermal cycles, and solidification parameters, numerical models can be employed. Numerical calculations provide a means to accurately predict melt depth and subsurface temperatures and thermal cycles. Furthermore, calculations of the dimensionless Pe number provide a means to understand how changes in laser processing parameters impact the dominant heat transfer mechanisms within the molten pool and, ultimately, the melt depth.

[1] G. K. Lewis and E. Schlienger, "Practical considerations and capabilities for laser assisted direct metal deposition," Mater. Des. **21**(4), 417–423 (2000).

[2] D. Clark, M. Whittaker, and M. Bache, "Microstructural characterization of a prototype titanium alloy structure processed via direct laser deposition (DLD)," Metall. Mater. Trans. B **43**, 388–396 (2012).

[3] G. P. Dinda, A. K. Dasgupta, and J. Mazumder, "Laser aided direct metal deposition of Inconel 625 superalloy: Microstructural evolution and thermal stability," Mater. Sci. Eng. A **509**, 98–104 (2009).

[4] L. Thijs, F. Verhaeghe, T. Craeghs, J. Van Humbeeck, and J.-P. Kruth, "A study of the microstructural evolution during selective laser melting of Ti–6Al–4V," Acta Mater. **58**, 3303–3312 (2010).

[5] K. K. B. Hon, L. Li, and I. M. Hutchings, "Direct writing technology— Advances and developments," CIRP Ann. **57**, 601–620 (2008).

[6] D. D. Gu, W. Meiners, K. Wissenbach, and R. Poprawe, "Laser additive manufacturing of metallic components: Materials, processes and mechanisms," Int. Mater. Rev. **57**(3), 133–164 (2012).

[7] H. Krauss, C. Eschey, and M. F. Zaeh, "Thermography for monitoring the selective laser melting process," in *Proceedings of the 23rd Annual International Solid Freeform Fabrication Symposium*, edited by D. Bourell, R. Crawford, C. Seepersad, J. Beaman, and H. Marcus (The University of Texas at Austin, Austin, TX, 2012).

[8] P. Aggarangsi, J. Beuth, and M. Griffith, "Melt pool size and stress control for laser based deposition near a free edge," in *Solid Freeform Fabrication Proceedings*, edited by D. Bourell, R. Crawford, J. Beaman, K. Wood, and H. Marcus (The University of Texas at Austin, Austin, TX, 2003).

[9] G. Bi, A. Gasser, K. Wissenbach, A. Drenker, and R. Poprawe, "Characterization of the process control for the direct laser metallic powder deposition," Surf. Coat. Technol. **201**, 2676–2683 (2006).

[10] I. Smurov, M. Doubenskaia, and A. Zaitsev, "Comprehensive analysis of laser cladding by means of optical diagnostics and numerical simulation," Surf. Coat. Technol. (2012), http://dx.doi.org/10.1016/j.sufrcoat.2012.10.053.

[11] S. Wen and Y. Shin, "Modeling of transport phenomena during coaxial laser direct deposition process," J. Appl. Phys **108**, 044908 (2010).

[12] X. He, J. Elmer, and T. DebRoy, "Heat transfer and fluid flow in laser microwelding," J. Appl. Phys. **97**, 084909 (2005).

[13] A. Robert and T. DebRoy, "Geometry of laser spot welds from dimensionless numbers," Metall. Mater. Trans. B **32**, 941–947 (2001).

[14] A. Arora, G. G. Roy, and T. DebRoy, "Unusual wavy weld pool boundary from dimensional analysis," Scr. Mater. **60**, 68–71 (2009).

[15] R. Rai, G. G. Roy, and T. DebRoy, "A computationally efficient model of convective heat transfer and solidification characteristics during keyhole mode laser welding," J. Appl. Phys. **101**, 054909 (2007).

[16] S. Kou, "Fluid flow and solidification in welding: Three decades of fundamental research at the University of Wisconsin," Weld. J. **91**, 287s–302s (2012).

[17] M. C. Tsai and S. Kou, "Marangoni convection in weld pools with a free surface," Int. J. Numer. Methods Fluids **9**, 1503–1516 (1989).

[18] S. Mishra and T. DebRoy, "Measurements and Monte Carlo simulation of grain growth in the heat affected zone of Ti-6Al-4V welds," Acta Mater. **52**, 1183–1192 (2004).

[19]R. Rai, J. W. Elmer, T. A. Palmer, and T. DebRoy, "Heat transfer and fluid flow during keyhole mode laser welding of Tantalum, Ti-6Al, 304l stainless steel and Vanadium," J. Phys. D.: Appl. Phys. **40**, 5753–5766 (2007).

[20]A. De and T. DebRoy, "A smart model to estimate effective thermal conductivity and viscosity in the weld pool," J. Appl. Phys. **95**(9), 5230–5240 (2004).

[21]X. He, T. DebRoy, and P. Fuerschbach, "Probing temperature during laser spot welding from vapor composition and modeling," J. Appl. Phys. **94**(10), 6949–6958 (2003).

[22]X. He, T. DebRoy, and P. Fuerschbach, "Composition change of stainless steel during micro-joining with short laser pulse," J. Appl. Phys. **96**(8), 4547–4555 (2004).

[23]S. V. Patankar, *Numerical Heat Transfer and Fluid Flow* (Hemisphere Publishing Corporation, New York, 1980).

[24]X. He, P. W. Fuerschbach, and T. DebRoy, "Heat transfer and fluid flow during laser spot welding of 304 stainless steel," J. Phys. D: Appl. Phys. **36**, 1388–1398 (2003).

[25]A. Raghavan, T. A. Palmer, and T. DebRoy, "Evolution of laser-fired aluminum-silicon contact geometry in photovoltaic devices," J. Appl. Phys. **111**, 024903 (2012).

[26]M. Picasso, C. F. Marsden, J.-D. Wagniere, A. Frenk, and M. Rappaz, "A simple but realistic model for laser cladding," Metall. Mater. Trans. B **25**, 281–291 (1994).

[27]R. W. McVey, R. M. Melnychuk, J. A. Todd, and R. P. Martukanitz, "Absorption of laser irradiation in a porous powder layer," J. Laser Appl. **19**(4), 214–223 (2007).

[28]S. Mishra, "Grain growth in the heat-affected zone of Ti-6Al-4V alloy welds: Measurements and Monte Carlo simulations," M.S. Thesis, Penn State University, 2003.